Supporting Information

for

Sensitive Detection of Nonfluorescent Solutes in Small Amounts of Diluted Aqueous Solutions Through Photothermally Induced Reflectivity Modulation at Glass/Aqueous Solution Interfaces

Shu-hei Urashima* and Ryoji Kusaka

Nuclear Science and Engineering Center, Japan Atomic Energy Agency (JAEA), Tokai, Ibaraki 319-1195, Japan.

1. Absorption spectrum of the new coccine solution
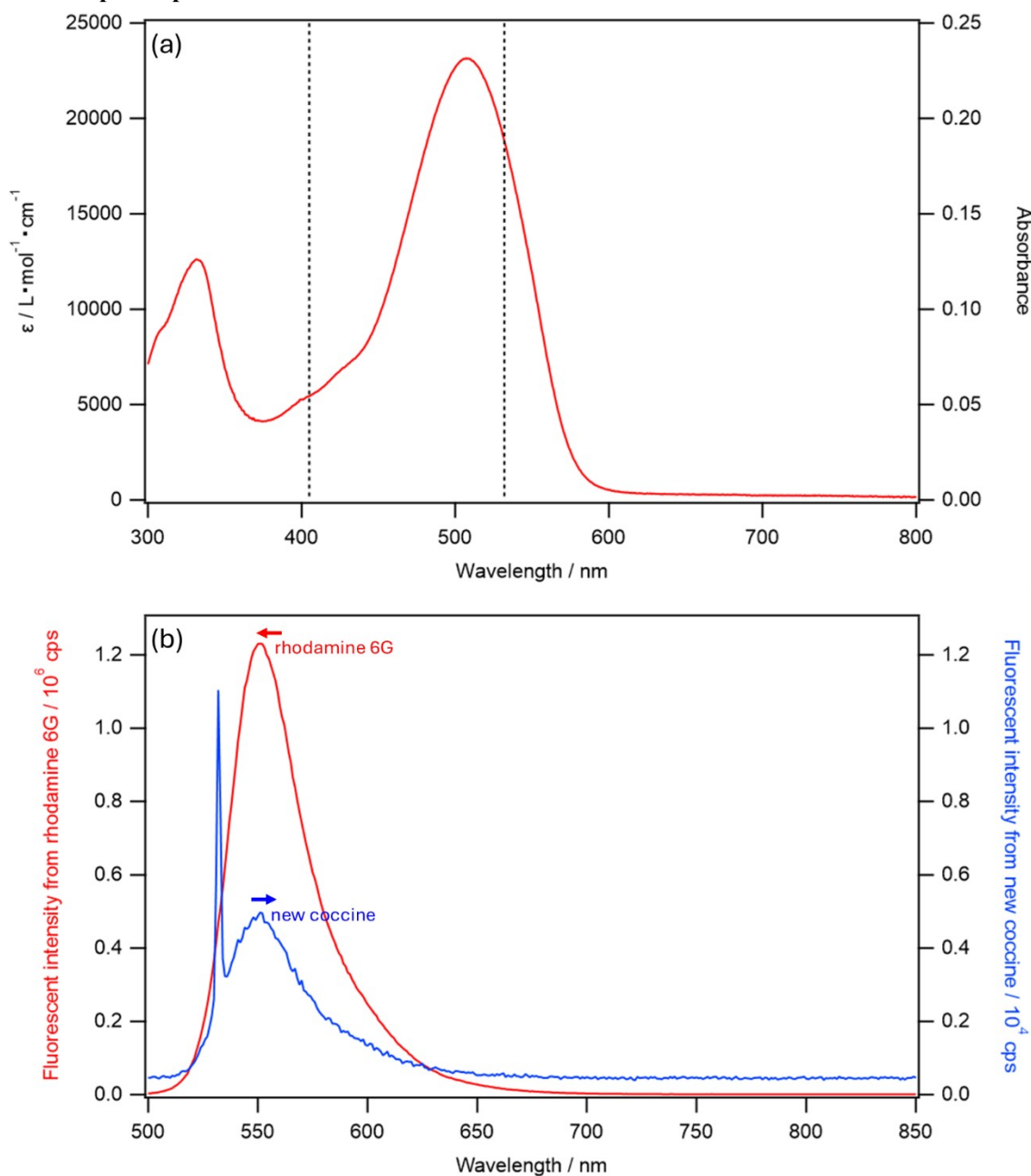
Figure S1. (a) Absorption spectrum of the new coccine solution measured with a commercial apparatus (Jasco, V-750). The concentration and the path length were 10 μM and 1 cm, respectively. The background was measured with pure water. The dotted lines are drawn at the probe and the pump wavelengths in the PTR measurement for eye guides. At these wavelengths, the molar absorptivity ε was 5400 and 18800 M^{-1} cm^{-1} for the probe and pump wavelengths, respectively. The peak was 507 nm, and ε at the peak was 23100 M^{-1} cm^{-1}. (b) The fluorescence spectra for 2 μM new coccine and rhodamine 6G aqueous solutions measured with a commercial apparatus (Horiba, FluoroMax-4). The excitation wavelength was 532 nm, and the monochromator slit widths for the excitation and fluorescence detection were 1 μm. The exposure time at each wavelength was 0.1 and 1 s for rhodamine 6G and new coccine, respectively. Note that the values for the vertical axes were 100 times different for rhodamine 6G and new coccine.

2. Experimental details for nanochannel

A nanochannel (380 nm deep and 50 μm wide) made with fused silica was used to demonstrate PTR measurements with nanometer-deep channels. The thickness of the glass substrates for the cell was 700 μm, and the channels were purchased from the Institute of Microchemical Technology as the microchannel used herein. According to the supplier, the channel was made by dry-etching, and the nanochannel depth was measured with a step gauge before bonding the substrates.

For the proof-of-principle experiment, the experimental procedure and the conditions were identical to those for the microchannel. For LOD determination, the procedure to replace the sample solution differed from that of the microchannel. Although only the solution inside was replaced for the microchannel, the nanochannel was removed from the sample stage every time the solution was replaced. Replacing the solution in the nanochannel required high pressure and could not be realized in our apparatus unless the cell was removed from the sample stage on the optical bench. Therefore, the optical conditions, especially the focused depth, should differ slightly for each concentration. The solution was replaced every two measurements, while at least four measurements were performed at the same concentration to evaluate how the replacement fluctuates the signal intensity.

3. Calculations for the performance evaluation and the proof of the principles

Estimation of the probe volume

The probe volume is derived for the micro- and nanochannels to determine the LOD. Since the temperature increase resulted from the pump beam, the focal volume of the pump beam corresponds to the probe volume.[1-9] First, since the beam diameter was matched with the objective lens pupil, the spot size of the focus point can be calculated from the NA of the objective lens by Gaussian optics. According to the literature,[9] the radius of the focus ω_0 is

$$\omega_0 = \frac{0.61\lambda}{NA}, \qquad (1)$$

where λ is the wavelength of the pump light. Similarly, the Rayleigh length z_r, a length between the focal point and a point where the cross-sectional area of the beam becomes twice the focal point, can be obtained as[9]

$$z_r = \frac{\pi\omega_0^2}{\lambda}. \qquad (2)$$

From NA = 0.70 and λ = 532 nm, ω_0 and z_r are calculated as 464 nm and 1270 nm, respectively. The focal volume is typically approximated by that of a cylinder whose radius and height are ω_0 and $2z_r$.[5, 6, 8, 10] With this approximation, the probing volume is estimated as $2\pi\omega_0^2 z_r = 1.7$ fL for the microchannel. Since the depth of the channel (380 nm) was thinner than the Rayleigh length, the height of the cylinder should be substituted with the depth, resulting in the probing volume of 0.26

fL for the nanochannel. Therefore, the concentrations of 1 nM and 6.4 nM correspond to 1 molecule in the probing volume for the micro- and nanochannels, respectively. Notably, for the microchannel, if the focus was perfectly adjusted at the glass/aqueous interface, half of the pumping cylinder is in the glass so that only the remaining half should contribute to the photothermal signal from the solution. Therefore, the probing volume would be 1.7/2 = 0.85 fL. However, it is challenging to ensure such an ideal alignment condition in the experiment. Since the smaller value of the probing volume might cause an unfairly small LOD estimation, the probing volume of 1.7 fL was adopted in this study. The LOD for the microchannels in this study is its worst limit in our experimental conditions.

Heat conduction simulation

In cylindrical coordinates, the heat conduction equation can be described as[11]

$$\frac{\partial}{\partial t}T(t,r,z) = \frac{k}{\rho c}\left[\frac{1}{r}\frac{\partial}{\partial r}\left(r\frac{\partial}{\partial r}\right) + \frac{\partial^2}{\partial z^2}\right]T(t,r,z) + \frac{Q}{\rho c}, \quad (3)$$

where T, k, ρ, and c are the temperature, the thermal conductivity, the density, and the specific heat capacity, respectively. Q is the heat generated by the light absorption in a unit time. The parameters t, r, and z are the time, radius, and the height in the cylindrical coordinate, respectively. Equation 3 assumes no azimuth dependence. Heat transfer by liquid convection and other flow reasons were neglected for simplicity. The heat source term Q was given in literature[7, 9] as

$$Q(r,z,t) = \frac{4P\varepsilon C}{\pi^2\omega_{pump}^2}\exp\left[-\varepsilon C\left(\frac{d_c}{2} - z\right)\right]\exp\left(-\frac{2r^2}{\omega_{pump}^2}\right) \times \frac{1}{2}(1 + \cos 2\pi ft), \quad (4)$$

where P, ε, C, d_c and f are the pump laser power, the molar absorptivity, concentration, the channel depth, and the modulation frequency of the pump laser, respectively. ω_{pump} is the radius at z,

$$\omega_{pump}^2 = \omega_0^2\left(1 + \frac{z^2}{z_r^2}\right). \quad (5)$$

In this study, Eq. 4 given by the literature was slightly modified as follows. First, the light decay term $\exp\left[-\varepsilon C\left(\frac{d_c}{2} - z\right)\right]$ was neglected for simplicity. Under the condition of ε = 18800 M^{-1}·cm^{-1} and C = 1 mM, light propagation of 2.5 μm ($2z_r$) only loses its power to 99%, so the neglect hardly affects the results. Further, while Eq. 4 assumes the pumping power is modulated sinusoidally, the optical chopper modulated the pump beam in our experiment, leading to stepwise modulation. Therefore, the modulation term $\frac{1}{2}(1 + \cos 2\pi ft)$ was substituted with a step function $s(t)$, which is 0 or 1 by changing its value every 1.43 ms. The value 1.43 ms was derived from the chopping frequency of 349 Hz, *i.e.*, it takes 1000/349 = 2.86 ms for 1 cycle, and hence $s(t)$ should change every half cycle of 1.43 ms. Consequently, Eq. 4 is rewritten as

4

$$Q(r,z,t) = \frac{4P\varepsilon C}{\pi^2 \omega_{pump}^2} \exp\left(-\frac{2r^2}{\omega_{pump}^2}\right) s(t). \quad (6)$$

Finally, since the pump laser was focused on the glass/aqueous interface, an offset z_f was introduced to z of Eq. 5 as

$$\omega_{pump}^2 = \omega_0^2 \left[1 + \frac{(z - z_f)^2}{z_r^2}\right]. \quad (7)$$

z_f is the focused depth, which was set at the point in the solution with z_r away from the glass–aqueous interface. As described in the probe volume estimation section, if the focus was perfectly set on the glass/aqueous interface, z_f should be just on the interface. The point z_r away from the glass/aqueous interface was adopted in this study for being consistent with the experimental assumption for the probing volume estimation. A numerical definition of z_f will be given after introducing the calculation box. Eq. 7 was employed for the microchannel simulation, and $\omega_{pump}^2 = \omega_0^2$ was assumed for calculating the nanochannel because its depth is much smaller than z_r.

Notably, if z_f is at the center of the channel, the laser size ω_{pump}^2 at the glass/water interface should increase only 2%, which is negligible in the current simulation accuracy.

The physical quantities k, ρ, and c were 0.610 W/m·K,[12] 997 kg/m³,[13] and 4182 J/kg·K[14] for the aqueous phase, respectively, and 1.27 W/m·K,[15] 2200 kg/m³,[16, 17] and 700 J/kg·K[18] for the glass phase, respectively. ε was 1880 and 0 m²/mol (i.e., 18800 and 0 M⁻¹ cm⁻¹) for the aqueous and glass phases, respectively.

As an initial condition for the FEM calculation, the temperature was uniformly set to 25 °C. In the calculation, the thickness of the water phase was assumed to be 100 μm and 380 nm for the micro- and nanochannels. $z = 0$ was defined as the center of the channels, and only the region of $z \geq 0$ was calculated. Namely, $z = 0$ was 50 μm and 190 nm below the glass–aqueous interface for the micro- and nanochannels, as depicted in Figure S2. Therefore, the focused depth for the microchannel was defined as $z_f = 50 - z_r = 48.73$ μm. At the edge of the calculation box, for aqueous side, no heat transfer in the z direction was assumed by introducing an assumption of $T_{i,0} = T_{i,1}$ for all i, where $T_{i,j}$ is the temperature at the ith r and jth z mesh. This assumption corresponds to mirror symmetry in the z direction. At the other edge of z (the glass side), $T_{i,j_{max}}$ was fixed to be 25 °C, so the heat at the edge can escape to outside the system. In the r-direction, no heat transfer was assumed at $r = 0$, namely $T_{0,j} = T_{1,j}$ was introduced. The temperature of the other edge of r (the region far from the pump light

focus), namely $T_{i_{max}j}$, was fixed to be 25 °C. At the glass/aqueous boundary, the temperature T_{i,j_b} was restricted to

$$T_{i,j_b} = \frac{k_{aq}T_{i,j_b-1} + k_{glass}T_{i,j_b+1}}{k_{aq} + k_{glass}} \qquad (8)$$

for all i, where k_{aq} and k_{glass} are the thermal conductivity of the aqueous and glass phases, respectively. The validation of the boundary condition (Eqn. 8) is given in the last of SI as an appendix. For the microchannel calculation, the thicknesses of the aqueous and glass phases were set to be 100 and 200 μm, respectively, and the mesh size and the time step were 500 nm and 500 ns, respectively. For the nanochannel calculation, the thicknesses were 380 nm and 24.8 μm for the aqueous and glass phases, respectively. The mesh size and the time step for the nanochannel calculation were 47.5 nm and 50 ns, respectively. The radial size of the calculation box was 50 and 9.5 μm for the microchannel and nanochannel, respectively. The simulation time is 3 ms, where one cycle of the pump irradiation with 349 Hz completes. Notably, the microchannel thickness calculated was lesser than that used in the experiment. However, as the channel depth dependence for the heat conduction behavior drastically changes only for the channel depth thinner than several micrometers,[7-9] the thickness of 100 μm in the calculation would be sufficient to estimate the heat flow in the thicker microchannels.

All calculations were performed using a lab-made program built on Igor Pro 9 software, using Eqns. 3, 6, and 7 under the parameters and the boundary conditions described above.

Optical simulation

The incident angle was assumed to be zero. For the nanochannel, since the upper (glass/aqueous) and lower (aqueous/glass) interfaces are included in the Rayleigh length, multireflection at these interfaces and optical interference of the reflected lights would contribute to the signal. The effective reflectivity R_{multi} at the interface considering the multireflection can be described as

$$R_{multi} = \left| r_{ga} + \frac{t_{ga}t_{ag}r_{ag}\exp(i\beta)}{1 - r_{ag}^2\exp(i\beta)} \right|^2 \qquad (9)$$

$$\beta = \frac{4\pi n d_c}{\lambda_{pr}}, \qquad (10)$$

where r_{xx} and t_{xx} are complex reflection and transmission coefficients, where the subscripts "ga" and "ag" represent the glass → aqueous and aqueous → glass directions, respectively. β is an optical phase shift occurring in each round-trip of the light in the aqueous phase. n and λ_{pr} are the refractive index of the aqueous phase and the probe beam vacuum wavelength, respectively. The derivation of Eqns. 9 and 10 is given at the last of the SI as appendix. Importantly, as the temperature rise changes r_{xx} and

t_{xx} through changing the refractive indices, it also changes the phase shift β. Therefore, by increasing the channel thickness d_c, the temperature effect would be enhanced if the upper and lower interfaces are in the Rayleigh length. Even at the same thickness, the phase-shift term would become notable when the number of the reflections inside the channel becomes large. In this study, since the refractive indices of water and glass are close, only one reflection at the upper and lower interfaces would be practically meaningful. To examine which reflectivity and phase shift primarily contribute to the modulation of the effective reflectivity, the thickness dependence under the multireflection condition was also simulated. Similarly, the probe wavelength dependence for the 380-nm channel was calculated.

In the calculation, the refractive indices of the aqueous[19] and glass[20] phases were 1.34269 and 1.46958, respectively, at the original temperature. Notably, the refractive index of pure H_2O was used for the aqueous phase, neglecting the perturbation due to the dye because the dye concentration considered is at highest 1 mM. The temperature coefficients of the refractive indices dn/dT were -9.1×10^{-5} and $+9.8 \times 10^{-6}$ K^{-1} for the aqueous[8] and glass[5] phases, respectively, neglecting temperature dependence of dn/dT. For the thickness dependence simulation, the temperature rise was assumed be 1 K.
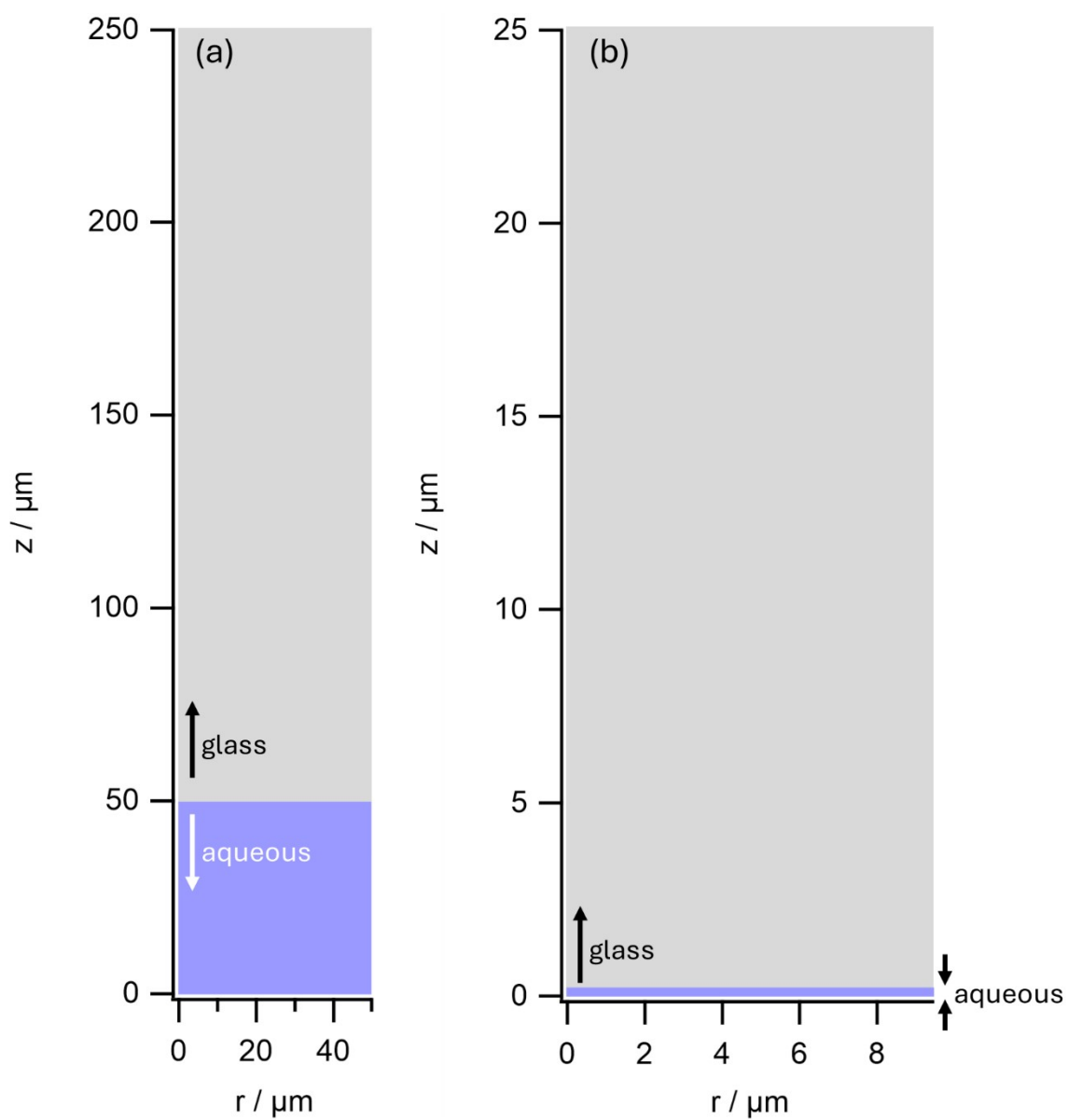
Figure S2. Calculation box for the thermal simulation for (a) microchannel and (b) nanochannel. The gray and blue parts represent the glass and aqueous phases.
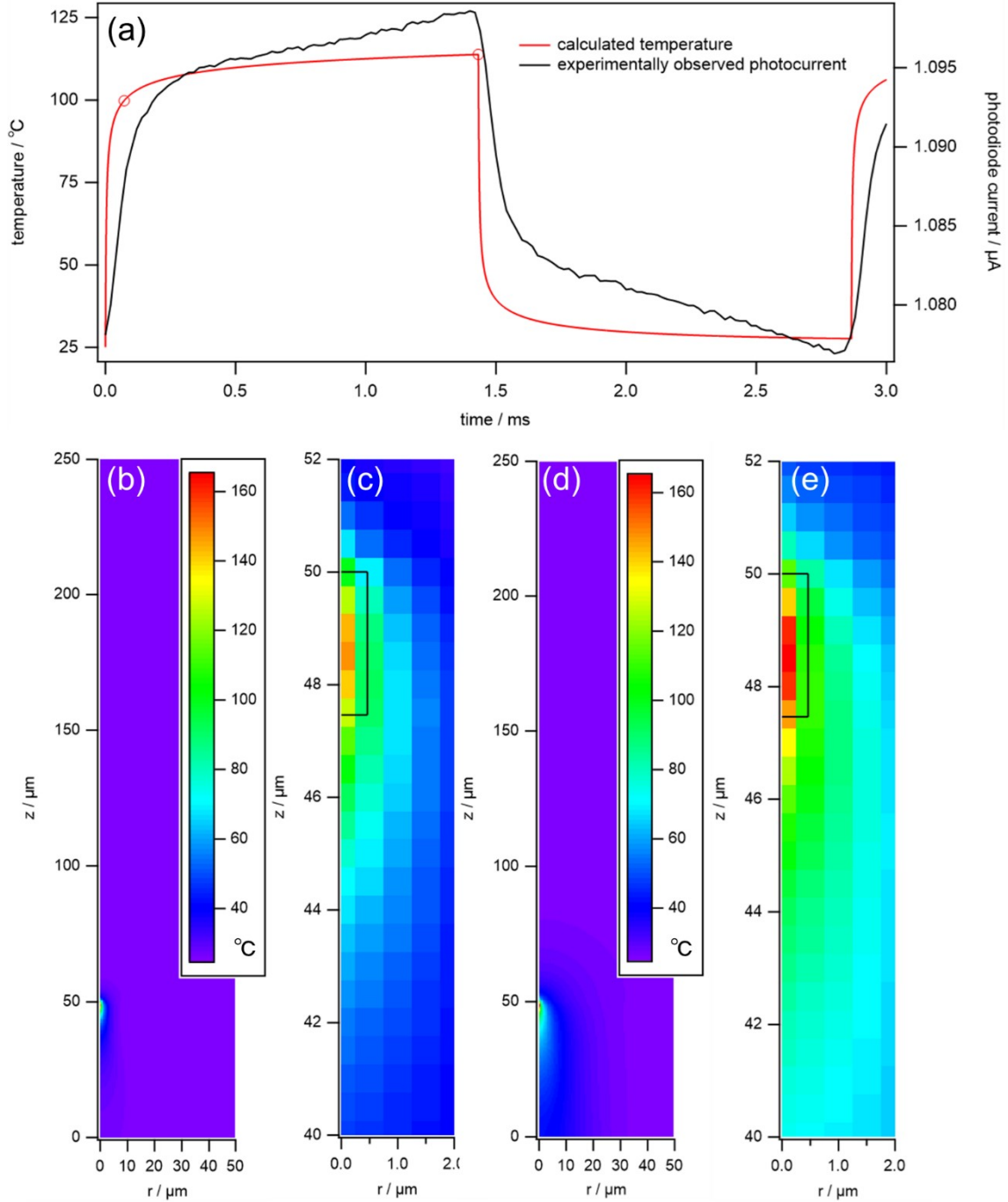
Figure S3. Results of the heat conduction simulation of the microchannel. The simulated concentration was 1 mM: (a) The time profile of the temperature at the center of the glass–aqueous interface ($r = 0$, $z = 50$ μm); the circle markers represent the moment at which the temperature distribution is shown in (b)–(e). The experimentally observed photodiode current (Figure 2(b) in the main text) was overlaid for comparison; (b, c) the temperature distribution at 72 μs (1/40 cycle); (d, e) that at 1.43 ms (1/2 cycle); (c) and (e) are the expansion of the (b) and (d) around the focus point, respectively; the black rectangles in (c, e) represents the probe volume defined by the focus radius ω_0 and the Rayleigh length Z_r.

4. Reflectivity enhancement under continuous excitation
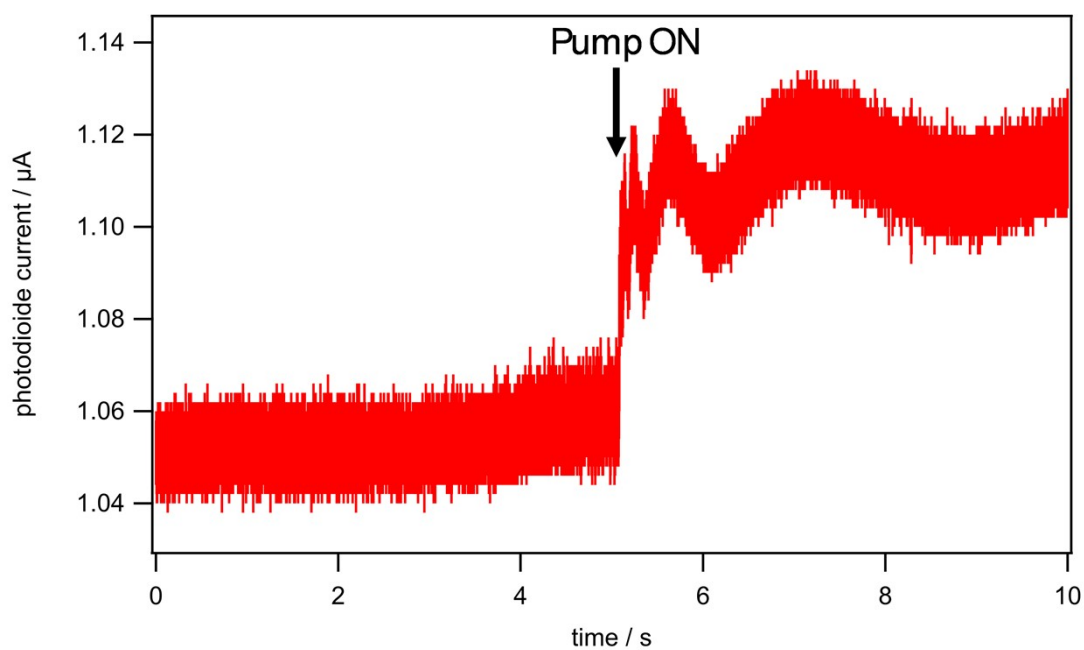
Figure S4. Photocurrent of PD1 with continuous irradiation of the pump beam without being chopped. The first 5 s were recorded without the pump to show the baseline level, and the pump beam started to be irradiated thereafter. The measurement was performed with 1 mM solution in the microchannel. The noise after opening the pump shutter was due to mechanical vibration of the optical table.

5. Results of proof-of-principle experiments and calculations for the nanochannel
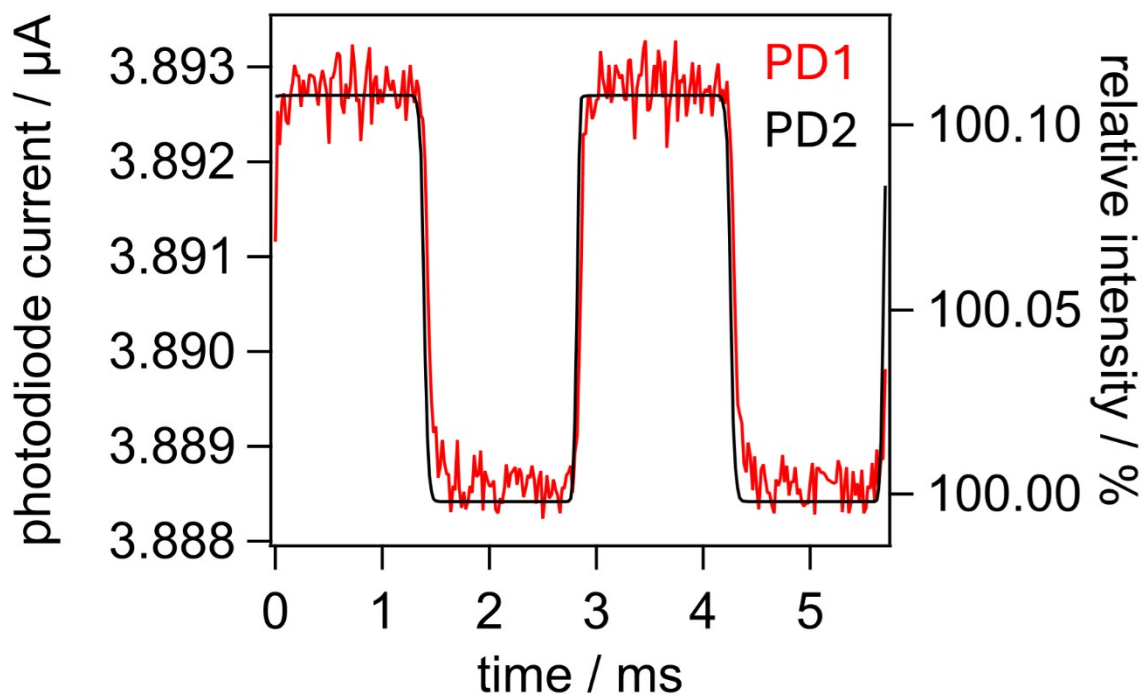
Figure S5. Photocurrent obtained for the nanochannel containing the 1-mM solution (2-cycle average); the current of PD2 is not scaled.
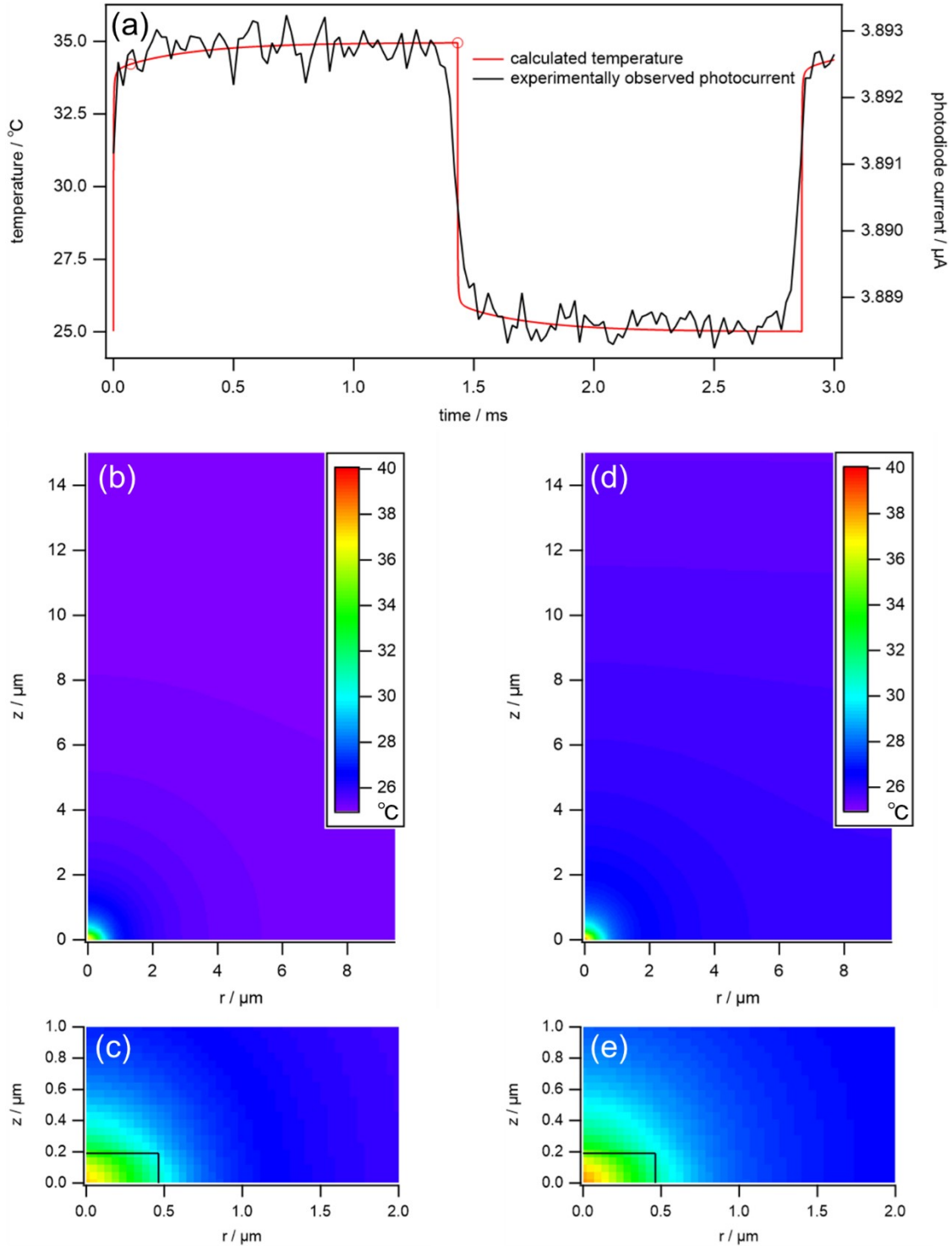
Figure S6. Results of the heat conduction simulation of the nanochannel. The simulated concentration was 1 mM. (a) The time profile of the temperature at the center of the glass–aqueous interface ($r = 0$, $z = 190$ nm). The circle markers represent the moment at which the temperature distribution is shown in (b)–(e). The experimentally observed photodiode current (Figure S5) was overlaid for comparison. (b, c) The temperature distribution at 72 μs (1/40 cycle). (d, e) That at the 1.43 ms (1/2 cycle). (c) and (e) are the expansion of the (b) and (d) around the focus point, respectively. The black rectangles in (c, e) represent the probe volume defined by the focus radius ω_0 and the channel depth.

12
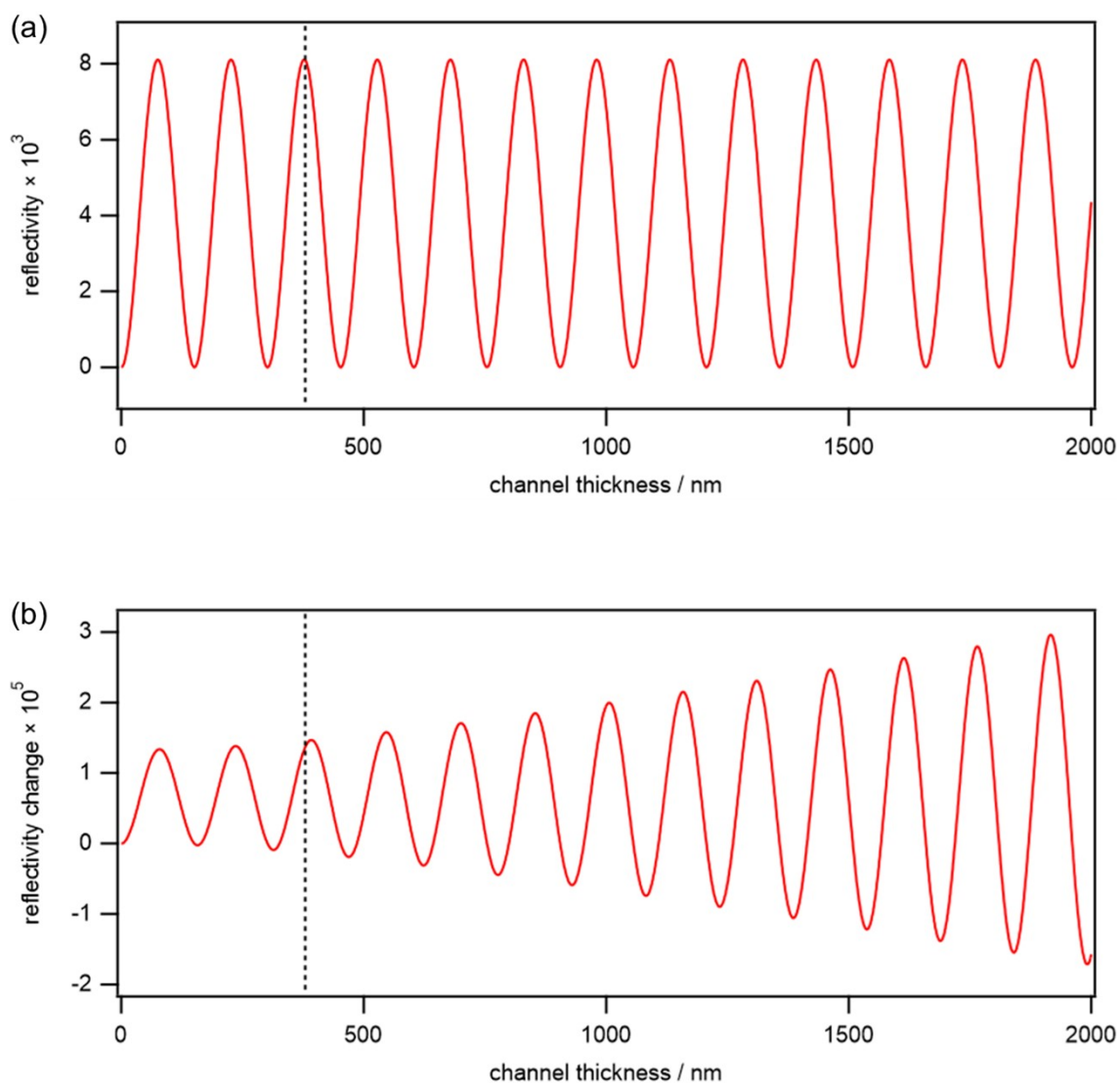
Figure S7. (a) Multireflection reflectivity of the glass nanochannel for the probe beam having the wavelength of 405 nm. (b) Change in the multireflection reflectivity upon the temperature rise of 1 K plotted against the channel thickness. It was calculated by $R_{ON} - R_{OFF}$, where R_{ON} and R_{OFF} are the reflectivity with and without the temperature rise, respectively. The vertical lines are drawn at 380 nm for eye guide. As shown in (b), while the reflectivity sinusoidally changed with the thickness due to the interference, the amplitude of the reflectivity change did not converge to zero, even at the thickness close to 0 nm, meaning the PTR signal with the nanochannel primarily originated in the reflectivity change, not the phase shift in the solution.

6. All data observed for the microchannel
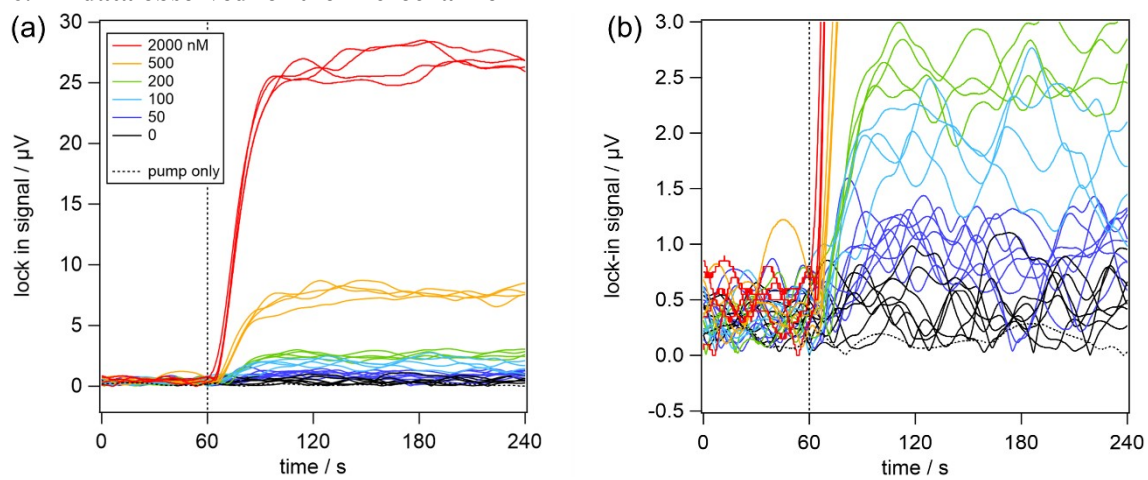
Figure S8. All data for the LOD determination of the microchannel measured in the identical optical conditions; (b) is the vertical expansion of (a).

7. Results of the LOD determination for the nanochannel
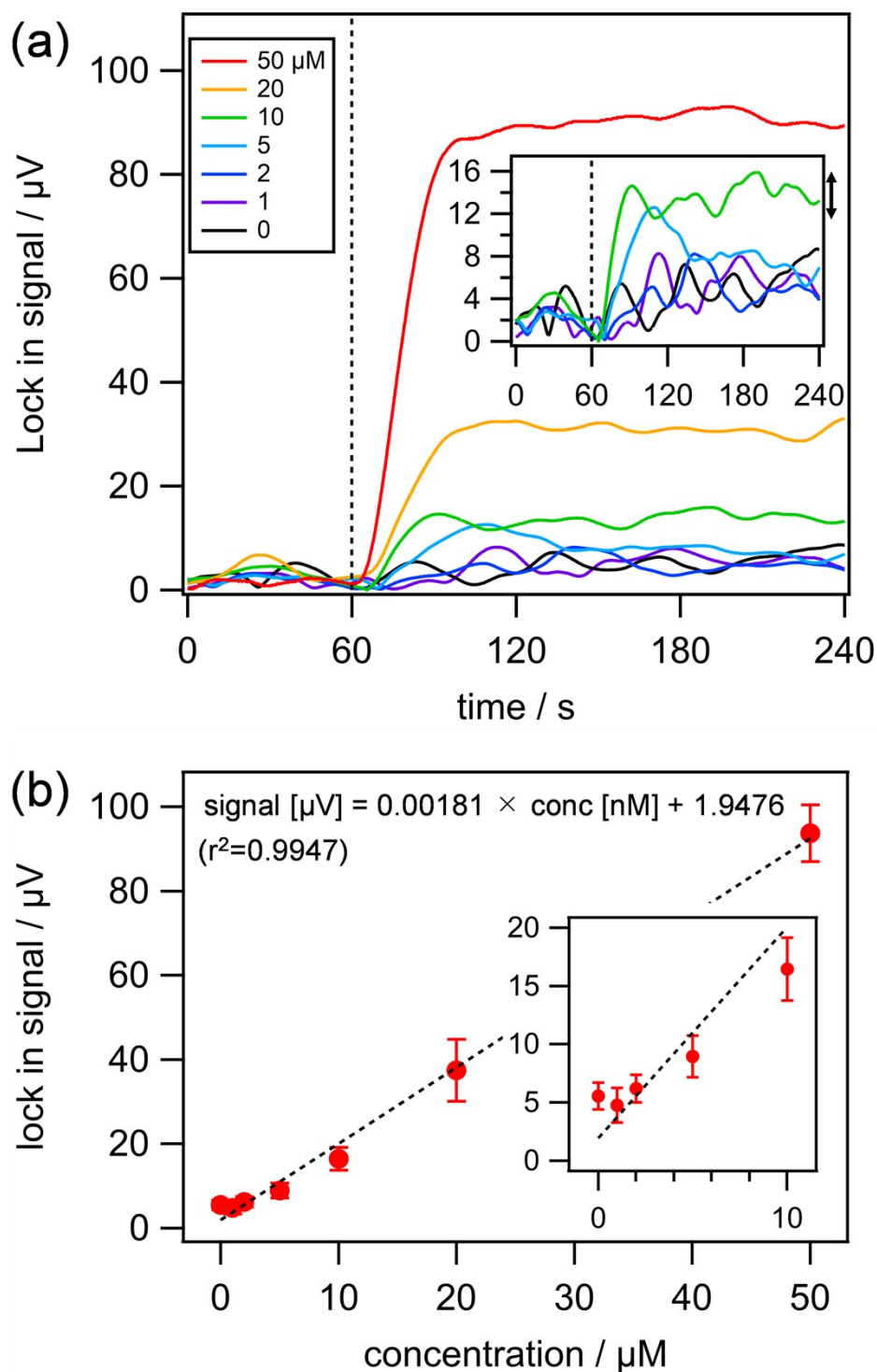
Figure S9. PTR signal obtained from the nanochannel. The insets are the expansion for the low concentration region. The axis labels for the insets were omitted and it is the same as the main panel. The data shown here are those least noisy, as in Figure 3 in the main text. All data are shown in Figure S10. (a) The raw PTR signal. The arrow near the inset represents the noise level. (b) The calibration curve of the PTR signal to the concentration. The dotted line is the linear fit. The limit of detection was 6 μM, corresponding to 1000 molecules.
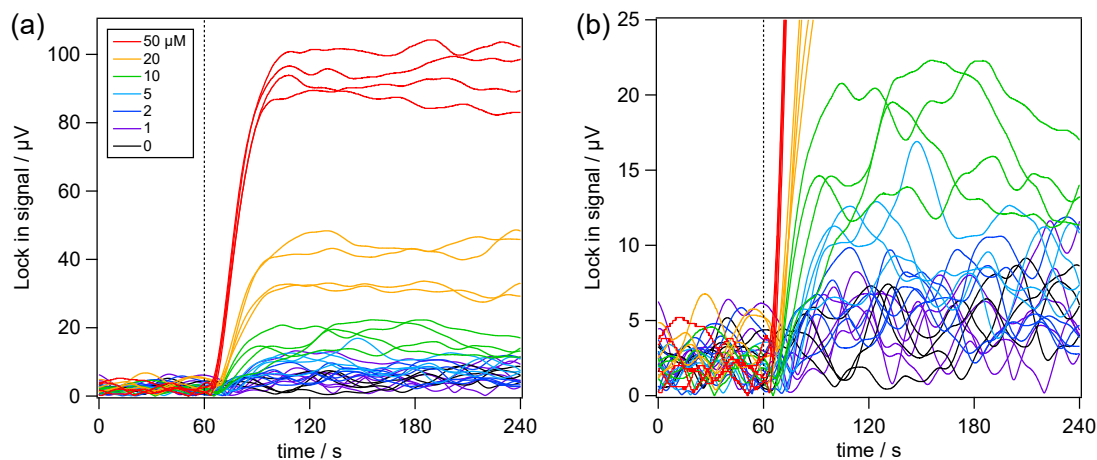
Figure S10. All data for LOD determination of the nanochannel measured in the identical optical conditions: (b) is the vertical expansion of (a). Note that, while the measurement cell was fixed on the stage and only the solution inside was replaced in the microchannel experiment, the nanochannel cell was removed from the stage every time the solution was replaced.

It should be noted that the signal intensities for the 3 lowest concentration (0-2 μM) were indistinguishable (the inset of Figure S9(b)) and the error bars (standard deviation) were much larger than those for the microchannel experiment (Figure 3(b) in the main text). Indeed, although there seems to be some difference for 0 and 2 μM in the raw data shown in Figure S10(b), it is not very clear. The reason for the worse results than the microchannel experiment is twofold. One is that, as depicted in the inset of Figure S9(a), the noise level is as high as 4 μV, which was equivalent to the baseline level for 0 μM data. The second is that, as described in the main text, the measurement cell replacement for the nanochannel experiment slightly varied the signal intensity. The effect of the replacement was most clear in the raw data for 20 μM in the Figure S10(a); approximately 45 μV was given in 2 of 4 measurement whereas only 30μV was in the other 2. The sudden change of the intensity indeed occurred when the cell was replaced.

Because the replacement varied the signal intensity, the standard deviation for the repeated measurement was worse than the microchannel experiment. Further, the deviation was worse for higher concentration, which is also because of the fluctuation by the cell replacement. Therefore, the measurement accuracy based on the standard deviation depends on the concentration. Approximately, the standard deviations were 2.5 and 7.5 μV for the concentrations up to 10 μM and higher, respectively. By using the slope of the calibration curve 0.00181 μV/nM, the measurement accuracies are calculated as ±1.4 and ±4.1 μM.

8. Calculations for prospect
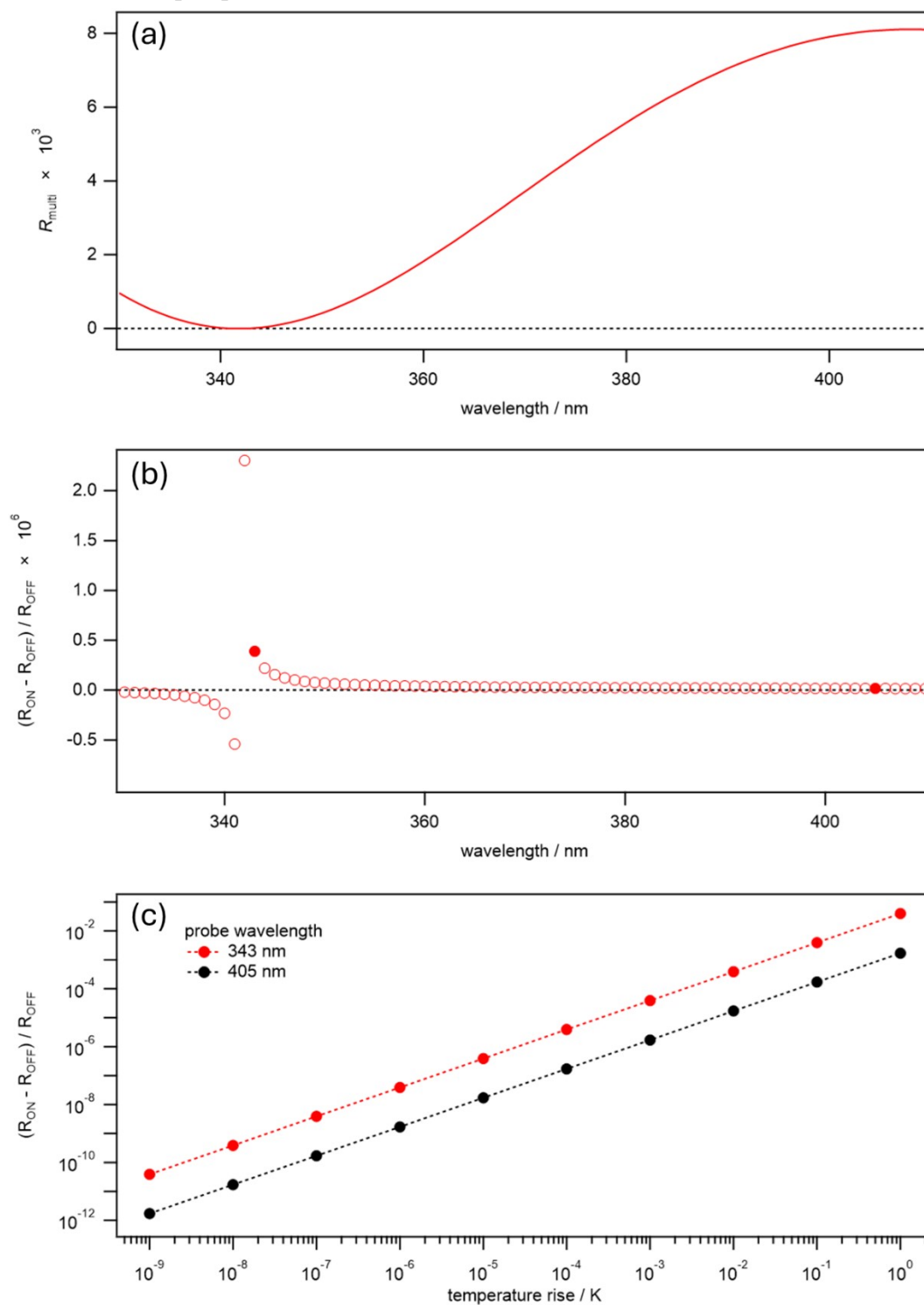
Figure S11. (a) Multireflection reflectivity of the 380-nm thick glass nanochannel plotted against the probe beam wavelength. (b) The modulation amplitude relative to the original signal intensity without the pump. The temperature rise of 10 μK was assumed. It was calculated by $(R_{ON} - R_{OFF})/R_{OFF}$, where R_{ON} and R_{OFF} are the reflectivity (R_{multi}) with and without the temperature rise, respectively. The markers for those at 343 and 405 nm are filled. (c) The relative modulation amplitude calculated for the probe lengths of 343 and 405 nm with the changing the rising temperature. All data shown in Figure S11 are simulated results.

17

9. Reference

[1] T. Kitamori, M. Tokeshi, A. Hibara, and K. Sato. *Anal. Chem.* 2004, *76* (3), 52a.

[2] M. A. Proskurnin, V. R. Khabibullin, L. O. Usoltseva, E. A. Vyrko, I. V. Mikheev, and D. S. Volkov. *Physics-Uspekhi* 2022, *65* (3), 270.

[3] E. Tamaki, A. Hibara, M. Tokeshi, and T. Kitamori. *J. Chromatogr. A* 2003, *987* (1-2), 197.

[4] E. Tamaki, A. Hibara, M. Tokeshi, and T. Kitamori. *Lab Chip* 2005, *5* (2), 129.

[5] T. H. Le, K. Mawatari, H. Shimizu, and T. Kitamori. *Analyst* 2014, *139* (11), 2721.

[6] H. Shimizu, K. Mawatari, and T. Kitamori. *Anal. Chem.* 2010, *82* (17), 7479.

[7] H. Shimizu, N. Miyawaki, Y. Asano, K. Mawatari, and T. Kitamori. *Anal. Chem.* 2017, *89* (11), 6043.

[8] H. Shimizu, S. Takeda, K. Mawatari, and T. Kitamori. *Analyst* 2020, *145* (7), 2580.

[9] H. Shimizu, and T. Kitamori. *Microfluid. Nanofluidics* 2021, *25* (7), 60.

[10] C. Chen, H. Shimizu, and T. Kitamori. *J. Opt. Microsyst.* 2021, *1* (02), 020901.

[11] D. W. Hahn, and M. N. Özisik. *Heat Conduction*, 3rd ed.; Wiley, New jersey, 2012.

[12] F. J. Dietz, J. J. De Groot, and E. U. Franck. *Bunsenges. Phys. Chem.* 2010, *85* (11), 1005.

[13] G. S. Kell. *J. Chem. Eng. Data* 2002, *20* (1), 97.

[14] D. C. Ginnings, and G. T. Furukawa. *J. Am. Chem. Soc.* 1953, *75* (3), 522.

[15] E. H. Ratcliffe. *Brit. J. Appl. Phys.* 1959, *10* (1), 22.

[16] H. Ye, X. Li, and C. Jiang. *Int. J. Appl. Glass Sci.* 2022, *13* (4), 664.

[17] B. T. Poe, C. Romano, and G. Henderson. *J. Non Cryst. Solids* 2004, *341* (1-3), 162.

[18] S. Belgacem, and H. Galai. Cement Refractory Bricks Characteristics: The Importance of Mineralogical Quantification in the Evaluation of the Refractory Bricks Corrosion. In *Refractory Materials: Characteristics, Properties and Uses*, Bryant, C. Ed.; Nova Science Pub Inc, NewYork, 2018.

[19] M. Daimon, and A. Masumura. *Appl. Opt.* 2007, *46* (18), 3811.

[20] I. H. Malitson. *J. Opt. Soc. Am.* 1965, *55* (10), 1205.

Appendix

A1. Validation of the boundary condition in Eqn. 8

Suppose a 1-dimensional structure in which two materials A and B having thermal conductivity of k_A and k_B are contacted as depicted in Figure S12. The lengths of the materials are l_A and l_B, and the edge temperature was fixed T_1 and T_2.
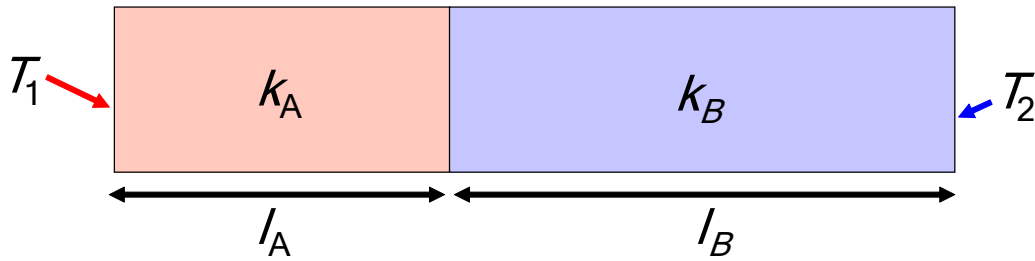
Figure S12. Schematic drawing of the simple 1-dimensional system considered.

Because no heat is generated, the 1-dimensional heat conduction equation is as follows:

$$\rho c \frac{\partial}{\partial t} T = k \frac{d^2}{dx^2} T.$$

Because $\frac{\partial}{\partial t} T = 0$ at the equilibrium, $\frac{d^2}{dx^2} T = 0$ is obtained. Therefore, T is written in the form of $T = ax + b$ for inside of each material. Therefore, by putting the temperature at the boundary of two materials as T_b, the temperature distribution is schematically depicted as Figure S13.
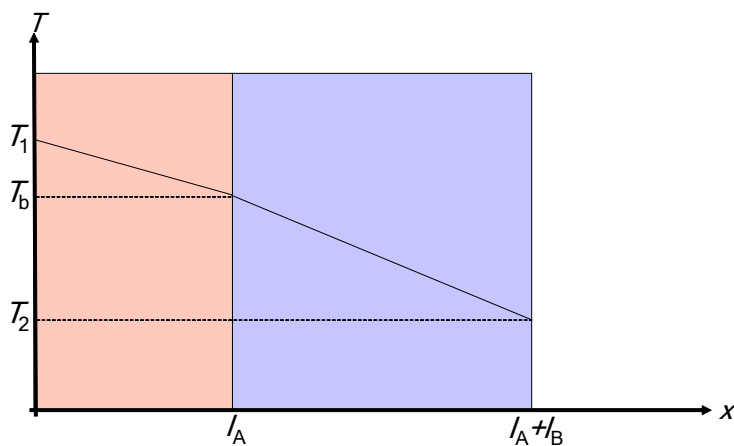
Figure S13. Schematic drawing of temperature distribution at the equilibrium.

Therefore, the following two equations

$$T(x) = -\frac{T_1 - T_b}{l_A}x + T_1$$

and

$$T(x) = -\frac{T_b - T_2}{l_B}(x - l_A) + T_b,$$

are obtained for inside the materials A and B, respectively. The remaining problem is to obtain T_b.

Because the heat flux q is derived as $q = -k\frac{d}{dx}T$ and the heat flux in the materials A and B must be equal at the equilibrium,

$$\frac{k_A(T_1 - T_b)}{l_A} = \frac{k_B(T_b - T_2)}{l_B}$$

is obtained. By solving this equation, we obtain:

$$T_b = \frac{l_B k_A T_1 + l_A k_B T_2}{l_A k_B + l_B k_A} \quad .$$

As an example, let us suppose the physical parameters for the materials A and B are those of water and glass, respectively, and the lengths of the material (l_A and l_B) are 0.2 and 0.8 mm. Namely, the physical quantities k, ρ, and c were 0.610 W/m·K, 997 kg/m³, and 4182 J/kg·K for the aqueous phase, respectively, and 1.27 W/m·K, 2200 kg/m³, and 700 J/kg·K for the glass phase. When the edge temperatures T_1 and T_2 are fixed at 100 °C and 0 °C, the boundary temperature T_b is calculated as

$$T_b = \frac{0.8 \times 0.610 \times 100 + 0.2 \times 1.27 \times 0}{0.2 \times 1.27 + 0.8 \times 0.610} = 65.8 \ [°C].$$

With knowing this analytical result, let us numerically calculate the temperature distribution. As an initial condition, the temperature was uniformly set at 10 °C. Three boundary conditions were examined: (1) $T_{j_b} = \dfrac{k_{aq}T_{j_b - 1} + k_{glass}T_{j_b + 1}}{k_{aq} + k_{glass}}$, (2) $T_{j_b} = \dfrac{T_{j_b - 1} + T_{j_b + 1}}{2}$, and (3)

$$T_{j_b} = T_{j_b}{}' + \Delta t\left[\frac{k_A}{\rho_A c_A}(\frac{T_{j_b + 1}{}' - 2T_{j_b}{}' + T_{j_b - 1}{}'}{(\Delta x)^2})\right]$$. Note that T_j in these equations represents the temperature at the jth mesh, and $T_j{}'$ represents that at 1 step before. The first one is the boundary condition used in the present study. The second is just an average of the closest meshes. In the third condition, the edge temperature was not specially treated at all and just calculated as the other mesh in the water phase. In the simulation, Δt and Δx were set at 0.5 μs and 1 μm, respectively.

Figure S14 shows the calculated results with the three boundary conditions. The system reached at the equilibrium at 3000001 steps so that the temperature distributions at 3000001 and

4900001 steps overlapped each other, regardless of the boundary condition. However, only the boundary condition (1) reproduced the theoretical result. Based on this preliminary calculation, we adopted the boundary condition (1) for the simulation. Because there is the glass/water boundary only in 1-dimensional z direction in our simulation box (Figure S2), the same boundary condition can be used although the simulations were indeed performed with the cylindrical coordinate.
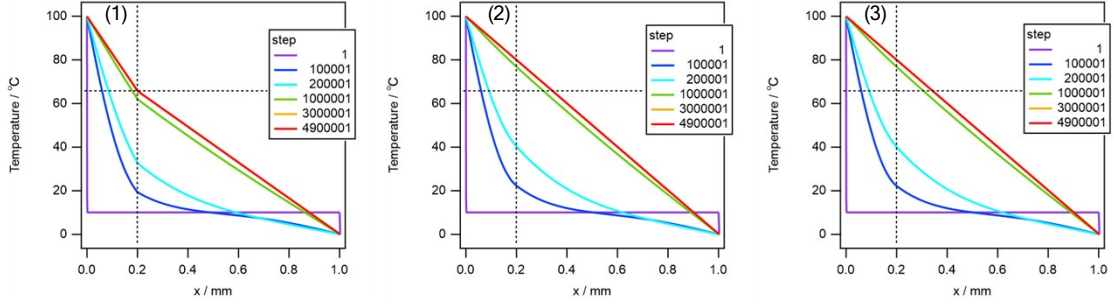
Figure S14. Calculated results with the boundary conditions (1)-(3). The vertical dotted lines represent the boundary position (water/glass interface) whereas the horizontal dotted lines are drawn at the theoretical temperature (65.8 °C) for eye guide.

A2. Derivation of Eqns. 9 and 10

Here, the equations

$$R_{multi} = \left| r_{ga} + \frac{t_{ga}t_{ag}r_{ag}\exp{(i\beta)}}{1 - r_{ag}^2\exp{(i\beta)}} \right|^2 \quad (9)$$

$$\beta = \frac{4\pi n d_c}{\lambda_{pr}}, \quad (10)$$

are derived under the normal incident (*i.e.*, incident angle is zero). As described previously, r_{xx} and t_{xx} are complex reflection and transmission coefficients, where the subscripts "ga" and "ag" represent the glass $\rightarrow$ aqueous and aqueous $\rightarrow$ glass directions, respectively. β is an optical phase shift occurring in each round-trip of the light in the aqueous phase. n and λ_{pr} are the refractive index of the aqueous phase and the probe beam vacuum wavelength, respectively.

First of all, the magnitude square in Eqn. 9 is to convert the coefficient of electric field to that of intensity. Because the intensity of the light is proportional to magnitude square of the electric field, R_{multi} is the form of magnitude square of effective reflection coefficient under the multireflection. Therefore, by writing the effective reflection coefficient at each reflection as r_n, R_{multi} is represented as

$$R_{multi} = \left| \sum_{n=0}^{\infty} r_n \right|^2 .$$

21

In this expression r_0 corresponds to the reflection coefficient for the first time, *i.e.*, the light reflected at the glass/water interface without entering to the aqueous phase. The schematic drawing for r_0, r_1, r_2 is shown in Figure S15.
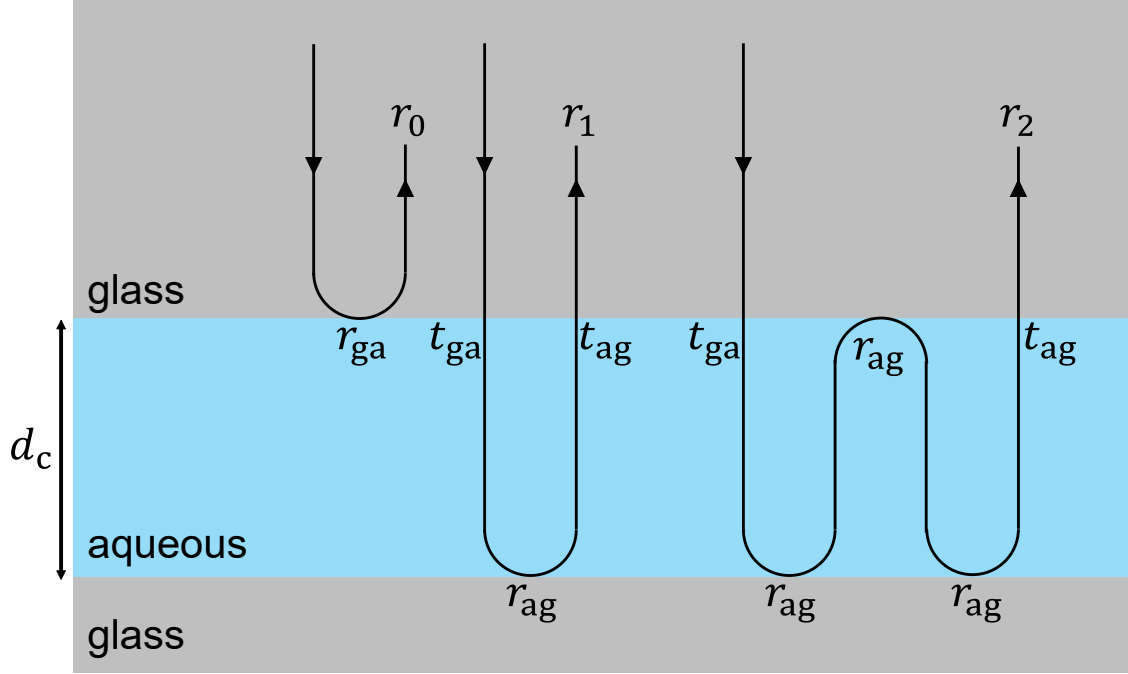
Figure S15. The schematic drawing of the multireflection.

From the figure, $r_0 = r_{ga}$ is obtained. r_1 is the effective reflectivity for the light once reflected at the aqueous/glass interface at the bottom. The light needs to (1) transmit to aqueous phase via the glass/aqueous interface, (2) reflect at the aqueous/glass interface, and (3) transmit to glass phase via the aqueous/glass interface. Further, the phase of the light must change by proceeding in the aqueous phase. Because the optical distance for 1 round-trip is $2nd_c$, the phase shift in radian is $2\pi \times \dfrac{2nd_c}{\lambda} = \dfrac{4\pi nd_c}{\lambda}$. As a result, by putting β as $\beta = \dfrac{4\pi nd_c}{\lambda}$ (Eq. 10), r_1 can be described as $r_1 = t_{ga}^{top} \times r_{ag}^{bottom} \times t_{ag}^{top} \times \exp(i\beta)$.

In this equation, the superscripts "top" and "bottom" were added to represent which interface the light reflects and transmits. Mathematically there is no difference between r_{ag}^{top} and r_{ag}^{bottom}. Similarly, r_2 is the effective reflectivity for the light twice reflected at the aqueous/glass interface at the bottom. Namely, $r_2 = t_{ga}^{top} \times r_{ag}^{bottom} \times r_{ag}^{top} \times r_{ag}^{bottom} \times t_{ag}^{top} \times \exp(2i\beta)$. Further, $r_3 = t_{ga}^{top} \times r_{ag}^{bottom} \times r_{ag}^{top} \times r_{ag}^{bottom} \times r_{ag}^{top} \times r_{ag}^{bottom} \times t_{ag}^{top} \times \exp(3i\beta)$. As a summary, for $n \geq 1$, r_n can be represented as

$$r_n = t_{ga} t_{ag} r_{ag} \exp{(i\beta)} \left[r_{ag}^2 \exp{(i\beta)} \right]^{n-1}.$$

Therefore, $r_n \ (n \geq 1)$ is a geometric progression having a first term of $t_{ga} t_{ag} r_{ag} \exp{(i\beta)}$ and a common ratio of $r_{ag}^2 \exp{(i\beta)}$. Generally, an infinite series S of a geometric progression having a first term of p and a common ratio of q is represented as

$$S = \frac{p}{1-q} \quad (if \ |q| < 1).$$

Using this equation, R_{multi} is represented as follows:

$$R_{multi} = \left| r_0 + \sum_{n=1}^{\infty} r_n \right|^2 = \left| r_{ga} + \frac{t_{ga} t_{ag} r_{ag} \exp{(i\beta)}}{1 - r_{ag}^2 \exp{(i\beta)}} \right|^2 \qquad (Eq. \ 9)$$